FUN3D Analyses in Support of the First Aeroelastic Prediction Workshop

Pawel Chwalowski,* Jennifer Heeg,†
Carol D. Wieseman‡ and Jennifer P. Florance§
NASA Langley Research Center, Hampton, VA 23681-2199

This paper presents the computational aeroelastic results generated in support of the first Aeroelastic Prediction Workshop for the Benchmark Supercritical Wing (BSCW) and the HIgh REynolds Number AeroStructural Dynamics (HIRENASD) configurations and compares them to the experimental data. The computational results are obtained using FUN3D, an unstructured grid Reynolds-averaged Navier-Stokes solver developed at NASA Langley Research Center. The analysis results for both configurations include aerodynamic coefficients and surface pressures obtained for steady-state or static aeroelastic equilibrium (BSCW and HIRENASD, respectively) and for unsteady flow due to a pitching wing (BSCW) or modally-excited wing (HIRENASD). Frequency response functions of the pressure coefficients with respect to displacement are computed and compared with the experimental data. For the BSCW, the shock location is computed aft of the experimentally-located shock position. The pressure distribution upstream of this shock is in excellent agreement with the experimental data, but the pressure downstream of the shock in the separated flow region does not match as well. For HIRENASD, very good agreement between the numerical results and the experimental data is observed at the mid-span wing locations.

Nomenclature

Roman Symbols

a	Source strength
c, c_{ref}	Chord length, chord reference length
C_p	Coefficient of pressure
M	Mach number
q	Dynamic pressure; generalized displacement
$\|\boldsymbol{r}\|$	Euclidean distance between a target point and a source
Re_c	Reynolds number based on chord
y^+	Dimensionless, sublayer-scaled wall coordinate of first node away from surface

Greek Symbols

α	Angle of attack
$\Delta\bar{s}$	Characteristic length (average mesh spacing)
Δs_0	Primary grid spacing at the source
$\Delta s_{\|\boldsymbol{r}\|}$	Primary grid spacing at the target point as a function of $\|\boldsymbol{r}\|$, Eqs. 2 and 3
Γ_1	Geometric rate of growth of grid spacing from a source

*Senior Aerospace Engineer, Aeroelasticity Branch, MS 340, Senior Member AIAA
†Senior Research Engineer, Aeroelasticity Branch, MS 340, Senior Member AIAA
‡Senior Research Engineer, Aeroelasticity Branch, MS 340, Associate Fellow AIAA
§Aerospace Engineer, Aeroelasticity Branch, MS 340

Γ_2	Exponential rate of growth of grid spacing from a source
η	Hybrid growth exponent
ω, f	Frequency - radians/second, Hz

Acronyms

AePW	Aeroelastic Prediction Workshop
BSCW	Benchmark Supercritical Wing
CAE	Computational Aeroelasticity
CFD	Computational Fluid Dynamics
DFT	Discrete Fourier Transform
DPW	Drag Prediction Workshop
FRF	Frequency Response Function
HIRENASD	HIgh REynolds Number AeroStructural Dynamics
HiLiftPW	High Lift Prediction Workshop
OTT	Oscillating Turntable
CSD	Cross Spectral Density
PSD	Power Spectral Density

I. Introduction

The fundamental technical challenge in Computational Aeroelasticity (CAE) is the accurate prediction of unsteady aerodynamic phenomena and their effects on the aeroelastic response of a vehicle. Currently, a benchmarking standard for use in validating the accuracy of CAE codes does not exist. Many aeroelastic data sets have been obtained via wind-tunnel and flight tests throughout the world; however, none have been globally presented or accepted as a standard data set. There are numerous reasons for this, including narrowly focused test objectives, insufficient data and/or test details, and experimental testing deficiencies. In addition, some existing data sets that might be excellent test cases for verifying certain regions of the CAE prediction landscape are proprietary to the organizations that obtained them, making them unavailable to the general CAE community. One test case that has been widely used by analysts for their validation efforts for more than 20 years is the AGARD 445.6 wing.[1,2] Although the results provide some insight into the prediction capabilities of the individual codes, the test case itself is limited in that many of its flutter data sets lack sufficient geometric or modal information for more extensive code validations, thus restricting its usefulness in the validation process.[3]

The accuracy of computational methods has improved in recent years due to individual validation efforts like those with the AGARD 445.6 wing, but multi-analyst code-to-code comparisons that can be used to assess the overall current state-of-the-art in CAE are limited. The idea for an Aeroelastic Prediction Workshop (AePW) series was conceived at NASA Langley Research Center in 2009, based on the success of two other workshop series that have been conducted over the past decade: the Drag Prediction Workshop (DPW)[4] series and the High Lift Prediction Workshop (HiLiftPW)[5] series. The intent for the AePW was to provide a forum for code-to-code comparisons involving predictions of nonlinear aeroelastic phenomena and to stimulate upgrades for existing codes and the development of new codes.

For code validations in general, the type of aerodynamic and/or aeroelastic phenomena to be analyzed is important since that validation process typically progresses from simpler to more challenging cases. For the AePW series, the approach being taken is to utilize existing experimental data sets in a building-block approach to incrementally validate targeted aspects of CAE tools. Each block will represent a component of a more complex nonlinear unsteady aeroelastic problem, isolating it such that the contributing physics can be thoroughly investigated. The challenge selected for the first AePW was the accurate prediction of unsteady aerodynamic phenomena and their effects on the aeroelastic

response of essentially rigid, geometrically simple models, with an additional foray into systems with weak coupling between the fluid and the structure. Results from this first workshop will help guide the direction of future workshops, with analyses extending to include predictions of static aeroelastic properties, limit-cycle oscillation (LCO), flutter, buffet, and control surface effectiveness with increasingly complicated flow fields and model geometries.

The AIAA AePW was held in conjunction with the 53rd AIAA Structures, Structural Dynamics, and Materials Conference on April 21-22, 2012, in Honolulu, Hawaii. The computational community was challenged to analyze three configurations and present their results at the workshop. The first two configurations involved rigid geometries in static and/or forced motion boundary conditions with attached, fully separated, and transiently separated flows at transonic conditions. The first configuration utilized the NASA Rectangular Supercritical Wing (RSW), which was tested in the NASA Langley Transonic Dynamics Tunnel (TDT) in 1982.[6–9] For this experiment, a simple, rectangular, rigid supercritical wing was sidewall mounted to a small splitter plate and oscillated in pitch, exhibiting a moderate shock and boundary-layer interaction. The second configuration utilized the NASA Benchmark Supercritical Wing (BSCW), which was tested in the TDT in 2000.[10] This data set was acquired for a rigid rectangular planform similar to the RSW that was sidewall-mounted to a large splitter plate assembly and oscillated in pitch via the TDT Oscillating Turntable (OTT), exhibiting a strong shock-induced separated flow at a moderate angle of attack. The third configuration considered for AePW extended the unsteady aerodynamic prediction to a weakly-coupled aeroelastic test case involving a more complex geometry: the HIgh REynolds Number AeroStructural Dynamics (HIRENASD) configuration. The HIRENASD model was tested in the European Transonic Windtunnel (ETW) in 2006.[11–13] For this experiment, a rigid, semi-span, transport-type wing configuration was mounted to the tunnel ceiling and oscillated at or near the frequency of the first bending mode, the second bending mode, or the first torsion mode.

The main focus of this paper will be presenting the computational aeroelastic results generated for the BSCW and HIRENASD configurations using the NASA Langley-developed computational fluid dynamics (CFD) software FUN3D[14] and comparing those results to the experimental data. Information relevant to the numerical method employed will be presented first, including grid generation, rigid steady flow analysis, dynamic aeroelastic analysis, and post processing. Details associated with the BSCW and HIRENASD analyses will then be presented.

II. Numerical Method

A. Grid Generation

Unstructured tetrahedral grids were used in this study. They were generated using VGRID[15] with input prepared using GridTool.[16] The tetrahedral elements within the boundary layer were converted into prism elements using preprocessing options within the FUN3D software. Equation 1 describes the grid point distribution normal to the body, where Δ_n is the normal spacing of the n^{th} layer, Δ_0 defines an initial cell height, and the variables r_1 and r_2 define the geometric growth rate and the exponential growth rate, respectively.

$$\Delta_n = \Delta_0[1 + r_1(1 + r_2)^{n-1}]^{n-1} \tag{1}$$

The off-surface length scale growth rate is governed by the parameters Γ_1 and Γ_2 according to the following equations:

$$\Delta s_{|\boldsymbol{r}|} = \Delta s_0 \left(1 + \frac{\Gamma_1}{a}\right)^{\eta} \tag{2}$$

where

$$\eta = \left(1 + \frac{|\boldsymbol{r}|}{\Delta\bar{s}}\Gamma_2\right) \frac{\ln\left(1 + \dfrac{|\boldsymbol{r}|\Gamma_1}{\Delta s_0 a}\right)}{\ln\left(1 + \dfrac{\Gamma_1}{a}\right)} \tag{3}$$

and Δs_0 is the primary grid spacing at the source, $\Delta s_{|\boldsymbol{r}|}$ is the primary grid spacing at the target point, η is the hybrid growth exponent, $|\boldsymbol{r}|$ is the Euclidean distance between a target point and a source, a is the source strength, and $\Delta\bar{s}$ is the characteristic length (average mesh spacing).[15]

Based on the AePW gridding guidelines,[17] three grids belonging to the same family were constructed. The magnitudes of the growth rate parameters, number of prism layers, grid sizes, and other grid parameters associated with the BSCW and HIRENASD analyses are shown in Tables 1 and 2, respectively.

Table 1. VGRID parameters for BSCW configuration grids based on Re_c = 4.49 * 10^6 and c_{ref} = 16.0 inch.

	Coarse	Medium	Fine
Chordwise Spacing at Wing LE	$0.17\%c_{root}$	$0.10\%c_{root}$	$0.06\%c_{root}$
Chordwise Spacing at Wing TE	$0.17\%c_{root}$	$0.10\%c_{root}$	$0.06\%c_{root}$
Average Cell y^+	1.000	0.667	0.444
Prism Layer Cells	30	30	30
Viscous Wall Spacing Δ_0 (inch)	$9.40E^{-5}$	$6.3E^{-5}$	$4.2E^{-5}$
Grid Size (nodes in millions)	3.0	9.0	27.0
Outer Boundary	$100c_{ref}$	$100c_{ref}$	$100c_{ref}$
Viscous Stretching r_1,r_2	0.02, 0.15	0.02, 0.15	0.02, 0.15
Γ_1,Γ_2	0.1, 0.1	0.1, 0.1	0.1, 0.1
Wind-Tunnel Ceiling Boundary Cond.	Symmetry	Symmetry	Symmetry

Table 2. VGRID parameters for HIRENASD configuration grids based on Re_c = 23.5 * 10^6 and c_{ref} = 0.3445 meter.

	Coarse	Medium	Fine
Chordwise Spacing at Wing LE	$0.17\%c_{root}$	$0.10\%c_{root}$	$0.06\%c_{root}$
Chordwise Spacing at Wing TE	$0.17\%c_{root}$	$0.10\%c_{root}$	$0.06\%c_{root}$
Average Cell y^+	1.000	0.667	0.444
Prism Layer Cells	30	30	30
Viscous Wall Spacing Δ_0 (meter)	$4.41E^{-7}$	$2.94E^{-7}$	$1.96E^{-7}$
Grid Size (nodes in millions)	6.4	19.1	56.3
Outer Boundary	$100c_{ref}$	$100c_{ref}$	$100c_{ref}$
Viscous Stretching r_1,r_2	0.02, 0.15	0.02, 0.15	0.02, 0.15
Γ_1,Γ_2	0.1, 0.1	0.1, 0.1	0.1, 0.1
Wind-Tunnel Ceiling Boundary Cond.	Symmetry	Symmetry	Symmetry

B. Rigid Steady-Flow Analysis

Solutions to the Reynolds-averaged Navier-Stokes (RANS) equations were computed using the FUN3D flow solver. Turbulence closure was obtained using the Spalart-Allmaras[18] one-equation model. For the transonic Mach numbers selected for the BSCW and HIRENASD analyses, flux limitation is not required; however, selected HIRENASD analyses were completed with and without flux limiter. Here, the flux limitation was accomplished with Venkatakrishnan[19] limiter. Inviscid fluxes were computed using the Roe scheme.[20] For the asymptotically steady cases under consideration, time integration was accomplished by an Euler implicit backwards difference scheme, with local time stepping to accelerate convergence. Most of the cases in this study were run for 10,000 iterations to achieve convergence of forces and moments to within $\pm 0.5\%$ of the average of their last 1,000 iterations.

C. Dynamic Analysis

Dynamic analyses of the BSCW and HIRENASD configurations required moving body and therefore grid motion capability. The grid deformation in FUN3D is treated as a linear elasticity problem. In this approach, the grid points near the body can move significantly, while the points farther away may not move at all. In addition to the moving body capability, the analysis of the HIRENASD configuration required dynamic aeroelastic capability. This capability is available in the FUN3D solver.[21] For structural dynamics analysis, FUN3D is capable of being loosely coupled with an external finite element solver,[22] or in the case of the linear structural dynamics used in this study, an internal modal structural solver can be utilized. This modal solver is formulated and implemented in FUN3D in a manner similar to

other Langley aeroelastic codes (CAP-TSD[23] and CFL3D[24]). For the HIRENASD computations presented here, the structural modes were obtained via a normal modes analysis (solution 103) with the Finite Element Model (FEM) solver MSC Nastran^{TM}.[25] Modes were interpolated to the surface mesh using the method developed by Samareh.[26]

The BSCW dynamic analysis was performed in a two-step process. First, the steady CFD solution was obtained on the rigid body. The BSCW wing was then moved sinusoidally along the pitch axis specified by the experiment. The HIRENASD dynamic analysis was performed in a three-step process. As with the BSCW analysis, the first step was to obtain the steady CFD solution on the rigid body. Next, a static aeroelastic solution was obtained by continuing the CFD analysis in a time accurate mode, allowing the structure to deform. A high value of structural damping (0.99) was used so the structure could find its equilibrium position with respect to the mean flow before the dynamic response was started. Finally, for the dynamic response, a user-specified modal motion was used. In this study, for harmonic perturbation, the modal displacement for mode n was computed as:

$$q_n = A_n sin(\omega_n t) \tag{4}$$

where A_n is amplitude, ω_n is frequency, and t is time.

D. Post Processing

The dynamic comparison data selected for AePW consisted of the magnitudes and phases of frequency response functions (FRFs). The frequency response functions of principal interest were the pressure coefficients (C_p) due to a selected displacement. The FRF for each pressure coefficient due to displacement was calculated at the principal frequency of the system response.

Fourier domain analysis was performed on each dynamically-excited data set to produce FRFs for each pressure relative to the displacement of the system. The FRFs were formed from power spectral and cross spectral densities (PSDs and CSDs), which were computed using Welch's periodogram method. The Fourier coefficients used in computing the PSDs and CSDs were generated using discrete Fourier transform (DFT) analysis of the time histories, employing overlap averaged ensembles of the data sets. The length of the ensembles and the frequency at which the data was extracted were chosen based on statistical analysis of the results of varying the ensemble lengths. The objective in varying the block size was to exactly match the system frequency with a Fourier analysis frequency and then maximize the number of data blocks to reduce the processing-based uncertainty. The block size for the final analysis was determined by minimizing the standard deviation among the periodograms of the peak of the PSD. In general, this gives slightly different frequency selection than would be obtained by a selection of the peak value of the PSD. In all cases, a rectangular window was used; the windows were overlapped by $75-95\%$ of the block size.

The displacement quantity, or reference signal, used depends on the configuration. For BSCW, the oscillatory pitch angle was the reference signal. For HIRENASD, the reference signal was the chord-normalized vertical displacement at a specified location.

For BSCW, the magnitude of the frequency response function of C_p due to θ at the frequency $f(i)$ as a function of chord location is presented in this paper as:

$$\left| \frac{C_p}{\theta}(f^*) \right| vs. \frac{x}{c} \tag{5}$$

For HIRENASD, the displacement used as the reference quantity was normalized by the reference chord. The magnitude of its FRF is presented as:

$$\left| \frac{C_p}{\frac{z}{c}}(f^*) \right| vs. \frac{x}{c} \tag{6}$$

III. Benchmark Supercritical Wing Computational Results

The second configuration posed for AePW utilized the BSCW configuration. This configuration was selected for several reasons. First, while it had similar geometric simplicity to the RSW configuration, the flow conditions were considered more challenging. The BSCW experiment exhibited highly nonlinear unsteady behavior, specifically shock-separated transient flow. Another reason for its selection was the availability and accessibility of all pertinent test information. The electronic data set is still available, including time history data records for all test conditions, the model still exists, making it available for inspection and retesting if desired, and the engineers who conducted the testing are also available for consultation regarding the model, test conditions, and data content. A third reason for

selecting the BSCW data set was that the test results were never extensively published. This data set was obtained twelve years ago during checkout testing of the new TDT OTT model support system and was therefore not the primary focus of a computational research project. Some data is available in graphical form,[10] but it is viewed as obscure enough to serve as the basis for a semi-blind test case. AePW analysts were not given the experimental data prior to the workshop.

The BSCW model, shown in Figure 1, has a simple, rectangular, 16- x 32-inch planform, with a NASA SC(2)-0414 airfoil. The model was mounted to a large splitter plate, sufficiently offset from the wind-tunnel wall (40 inches) to (1) place the wing closer to the tunnel centerline and (2) be outside the tunnel wall boundary layer.[27] It was designed to be rigid, with the following structural frequencies for the combined installed wing and mounting system: 24.1 Hz (spanwise first bending mode), 27.0 Hz (in-plane first bending mode), and 79.9 Hz (first torsion mode). Boundary-layer transition was fixed at 7.5% chord via a transition strip created using size 30 grit. For instrumentation, the model is capable of having two chordwise rows of 40 in-situ unsteady pressure ports at the 60% and 95% span locations, with 22 ports on the upper surface, 17 ports on the lower surface, and 1 port at the leading edge for each row. For the OTT checkout test, however, only the inboard row at the 60% span station was fully populated.

For the BSCW test on the OTT, data was acquired in both R-134a and air test mediums at Mach numbers ranging from 0.4 to 0.85, dynamic pressures (q) of 100, 170, and 200 psf, and angles of attack from -1 to 5 degrees. Dynamic data was obtained by oscillating the model in pitch about the 30% chord over a range of frequencies from 1 to 30 Hz. For AePW configuration number two, only data obtained in R-134a at Mach = 0.85, q = 200 psf, and $\alpha = 5$ degrees was used. This M/q combination fixed the Reynolds number at 4.49 million based on the wing chord, while the M/α combination was selected for its transient attached and separated flows.

Three test cases were selected for the BSCW computational challenge. The first was a steady case at the selected flow condition. It should be noted that for this test case, the experimental steady data was calculated as the mean value from the oscillatory time histories. To demonstrate the ability of the AePW computational methods to properly capture frequency effects, two dynamic cases were chosen as well. Both involved pitch oscillations of 1 degree about the $\alpha = 5$ degree mean. The frequencies of interest were 1 Hz and 10 Hz. These were chosen to minimize the potential structural coupling that could occur at the higher oscillation frequencies. A summary of the BSCW test cases is provided in Table 3.

In the following sections of this paper, the FUN3D computational results obtained for the AePW BSCW test cases will be presented with the corresponding experimental data. The rigid body solution will be discussed first, followed by the dynamic solution.

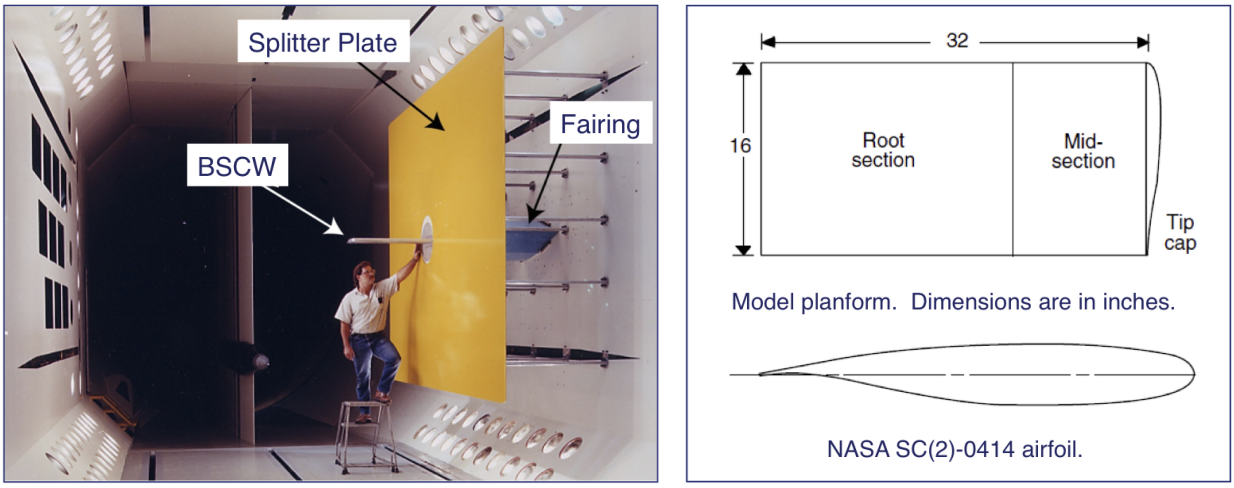

(a) Photograph of the BSCW model mounted in the TDT.

(b) BSCW geometry.

Figure 1. BSCW model.

A. Rigid-Body Solution

The rigid-body analysis at $\alpha = 5$ degrees showed a mixture of steady and unsteady flow, depending on the grid resolution. While the coarse-grid simulation converged to a steady state, the medium- and fine-grid solutions were unsteady. It is believed that the shock and the shock-induced boundary layer separation aft of the shock were the

Table 3. BSCW Analysis Test Cases.

Test Case	Mach No.	Mean α (deg)	Pitch Osc. Freq. (f, Hz)	Pitch Osc. Amp. (θ, deg)	Reduced Freq. ω c / $2V_\infty$	Re_c *10^6
1	0.85	5.0	0	0.0	0.000	4.49
2	0.85	5.0	1	1.0	0.009	4.49
3	0.85	5.0	10	1.0	0.090	4.49

cause of the unsteadiness in the steady state solution. The unsteady analysis with the rigid body produced the same unsteadiness in solution. The computed average aerodynamic coefficients for three grids are presented in Table 4.

Table 4. BSCW Analysis Aerodynamic Coefficients.

Grid	C_L	C_D	C_M
Coarse	0.4338	0.0757	-0.0376
Medium	0.4168	0.0752	-0.0341
Fine	0.3892	0.0741	-0.0259

B. Dynamic Solution

As mentioned previously, two unsteady forced-pitch oscillation cases were investigated, one at 1 Hz and the second at 10 Hz, both with a pitch amplitude of 1 degree. For the coarse-grid solutions FUN3D was run with 128 time steps per cycle. For the medium-grid solutions, 256 and 128 time steps per cycle were used for the 1 Hz and 10 Hz cases, respectively. For the fine-grid solutions, 1024 time steps per cycle were used. The coarse- and medium-grid solutions were run for six cycles, while the fine-grid solutions were run for two cycles. In all cases, the temporal convergence level was set to 5% and the number of subiterations was set to 75. For all but one solution, convergence was achieved within 75 subiterations. The fine grid solution at the 1 Hz forcing frequency did not converge. However, due to time and resource constraints, this solution was not rerun with an increased number of subiterations.

Figures 2(a)-(g) and 3(a)-(g) show the BSCW computational results generated for the 1 Hz and 10 Hz pitching frequencies, respectively. Figures (a) and (b) show the computed and experimental mean pressure on the upper and lower wing surfaces. The numerically-computed shock location on the upper surface is approximately 0.8 inches aft of the experimental shock. There is very good agreement in pressure upstream of the shock and poor agreement aft of the shock. This poor agreement aft of the shock may be attributed to the inability of the RANS solver to correctly compute flow physics in the separated-flow region. On the other hand, the resolution of pressure taps on the lower surface is too sparse to capture shock location. Figures (c) and (d) show the magnitude of the FRF of pressure due to displacement, and Figures (e) and (f) show the corresponding phase of the FRF. The FRF results confirm that the computed shock location on the upper surface is approximately 0.8 inches aft of the experimental shock location. Figure (g) shows the computed lift and drag coefficients. It should be noted that for the coarse and medium grids, the aerodynamic coefficients exhibit smooth sinusoidal behavior, while for a fine grid, the curves become more jagged. These jagged lift coefficient curves can be explained by looking at the computed pressure time histories at the four points on the wing shown in Figure 4. For the fine-grid solutions, the pressure time histories show similar jagged behavior in the separated flow regions, points 2 and 4. Upstream of the shock, points 1 and 3, pressure time histories show sinusoidal behavior.

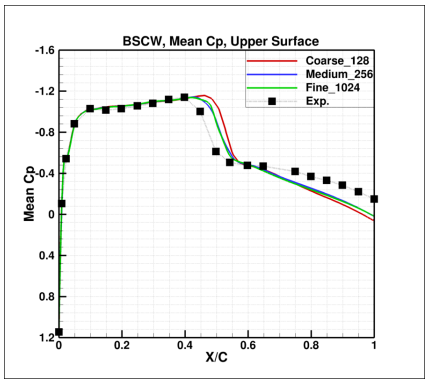

(a) Mean C_p, f = 1 Hz, Upper Surface.

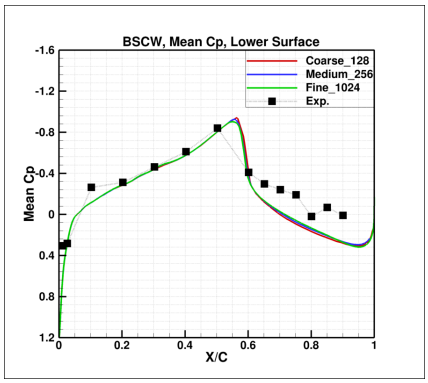

(b) Mean C_p, f = 1 Hz, Lower Surface.

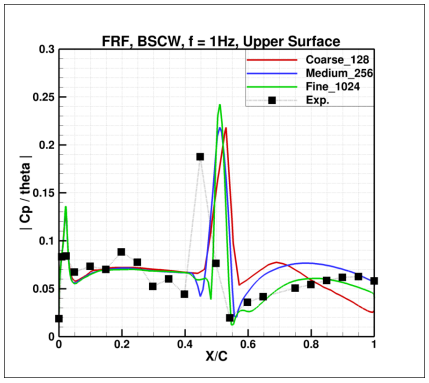

(c) | C_p/theta |, Upper Surface.

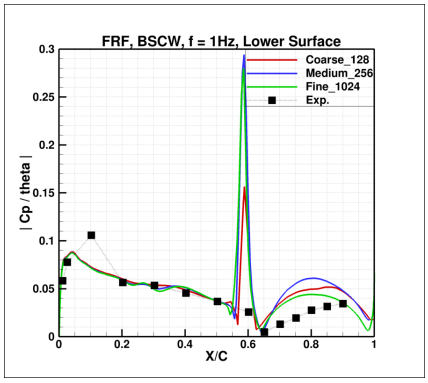

(d) | C_p/theta |, Lower Surface.

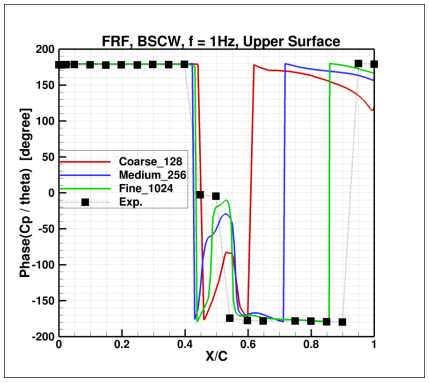

(e) Phase C_p/theta, Upper Surface.

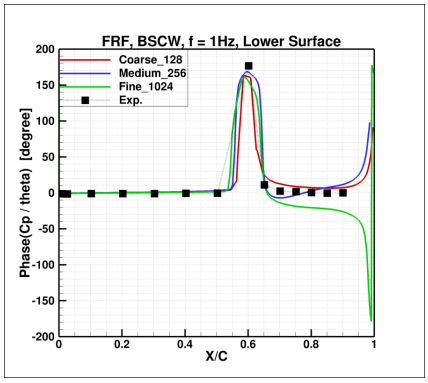

(f) Phase C_p/theta, Lower Surface.

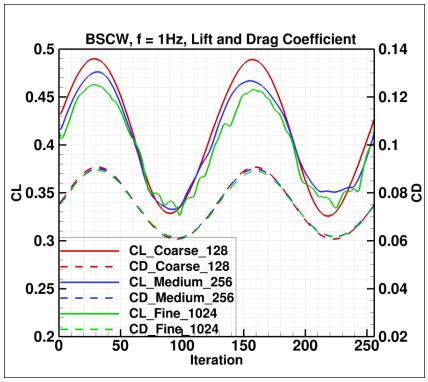

(g) Lift and Drag Coef.

Figure 2. Mean C_p and Frequency Response Function: Magnitude and phase of pressure due to pitch angle and aerodynamic coefficients, BSCW, Mach = 0.85, pitching frequency f = 1 Hz case.

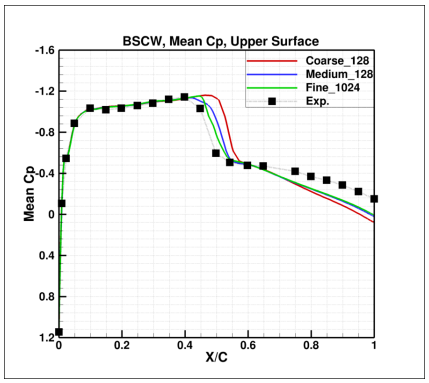

(a) Mean C_p, f = 10 Hz, Upper Surface.

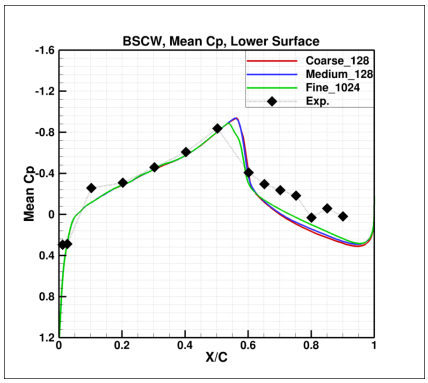

(b) Mean C_p, f = 10 Hz, Lower Surface.

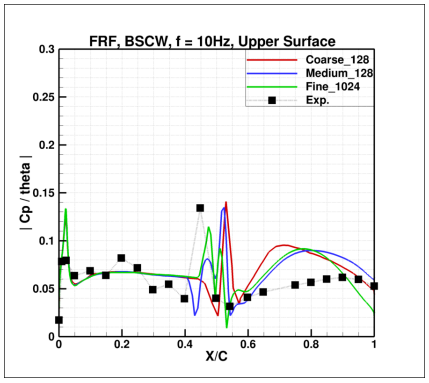

(c) | C_p/theta |, Upper Surface.

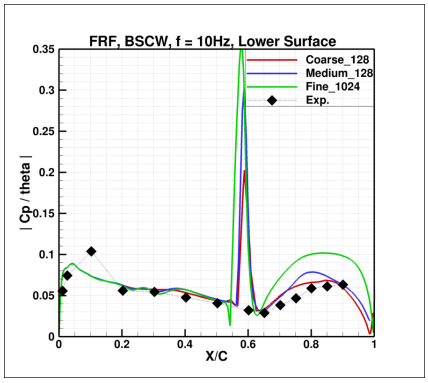

(d) | C_p/theta |, Lower Surface.

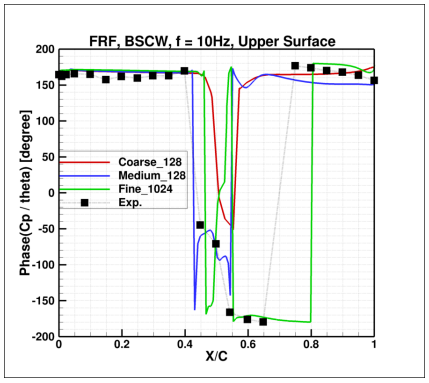

(e) Phase C_p/theta, Upper Surface.

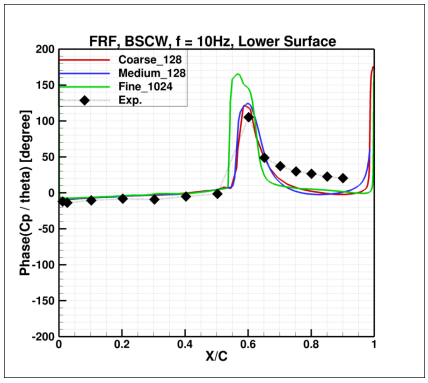

(f) Phase C_p/theta, Lower Surface.

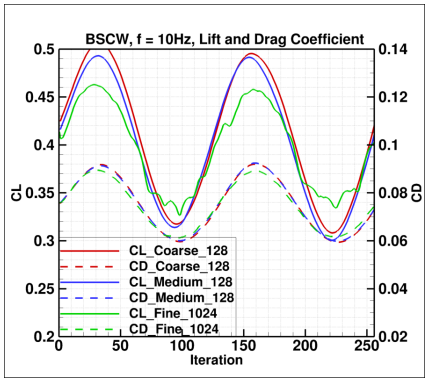

(g) Lift and Drag Coef.

Figure 3. Mean C_p and Frequency Response Function: Magnitude and phase of pressure due to pitch angle and aerodynamic coefficients, BSCW, Mach = 0.85, pitching frequency f = 10 Hz case.

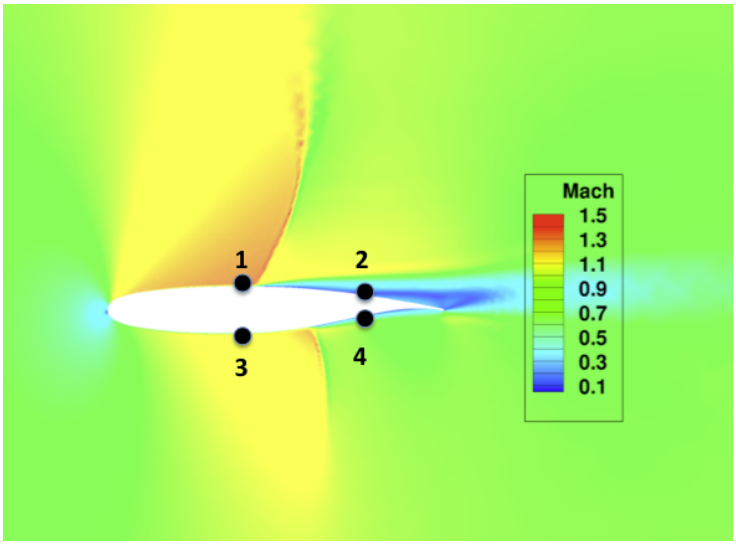

(a) Mach contour and location of four points with extracted pressure time histories.

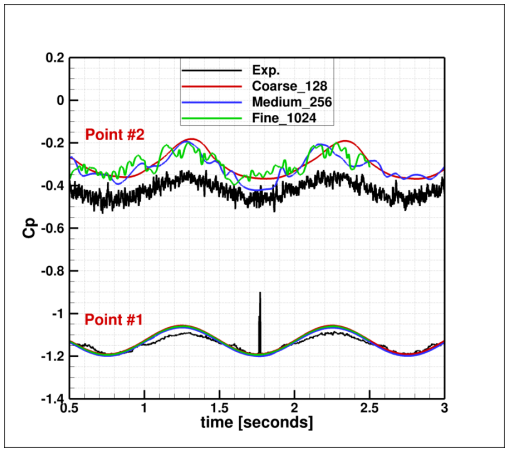

(b) Pressure time histories at points 1 and 2 on upper surface, 1 Hz test case.

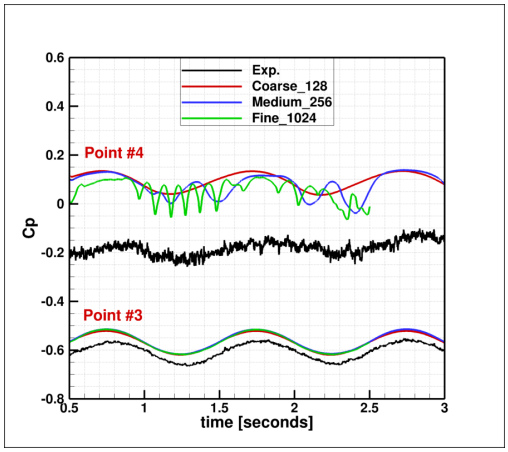

(c) Pressure time histories at points 3 and 4 on lower surface, 1 Hz test case.

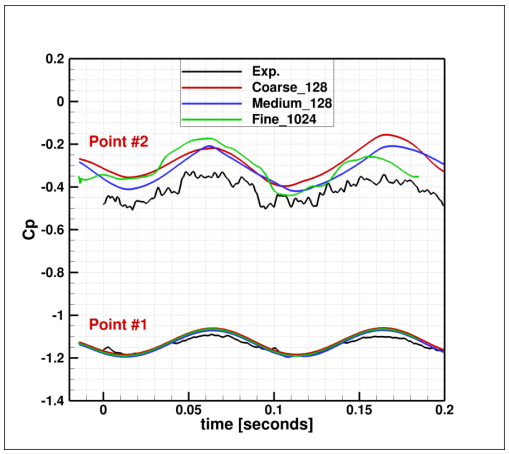

(d) Pressure time histories at points 1 and 2 on upper surface, 10 Hz test case.

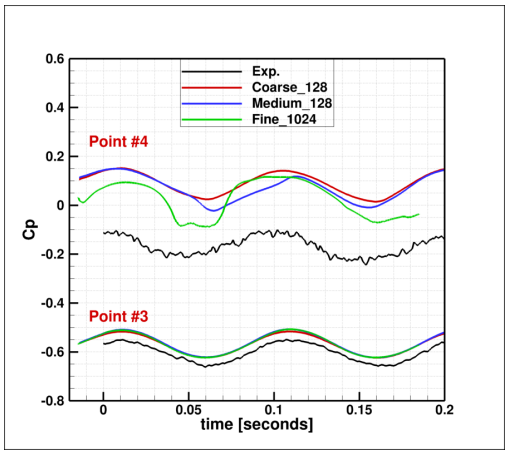

(e) Pressure time histories at points 3 and 4 on lower surface, 10 Hz test case.

Figure 4. BSCW pressure time histories at selected points on the wing for 1 Hz and 10 Hz cases.

IV. HIRENASD Computational Results

The third and final configuration considered for AePW involved the HIgh REynolds Number AeroStructural Dynamics (HIRENASD) Project[11–13] model. As mentioned previously, this model was chosen as the initial workshop foray into aeroelastic analysis of systems with weak coupling between the fluid and the structure. The HIRENASD wing has both a high degree of structural stiffness and widely-spaced structural modes, resulting in the weak aeroelastic coupling desired for configuration three. Another reason for selecting this configuration was the availability of both (1) the time histories for the complete data set and (2) the expertise from the engineers who performed the test and who have subsequently served as members of the AePW Organizing Committee. The final reason for choosing to analyze the HIRENASD configuration as part of AePW was that only a subset of the entire data set had been previously analyzed, distributed, and/or published. The data selected for AePW was included in this publicly-available subset, a situation viewed as beneficial for easing into the initial aeroelastic analyses since many of the analysts were already familiar with it. However, the complete HIRENASD data set is much more extensive and includes points that, while considered to be phenomenologically more complex that desired for AePW, have excellent potential for more advanced blind validation efforts at future workshops.

The HIRENASD Project was led by Aachen University′s Department of Mechanics with funding from the German Research Foundation. It was initiated in 2004 to produce a high-quality transonic aeroelastic data set at realistic flight Reynolds numbers for a large transport-type wing/body configuration and was tested in the European Transonic Windtunnel (ETW) in 2006. The HIRENASD wing planform, shown in Figure 5a, is a ceiling-mounted, semi-span, clean-wing configuration with a leading-edge sweep of 34 degrees, a span of approximately 1.3 meters, and a mean aerodynamic chord of 0.3445 meters. It consists of three sections. The two outboard sections use an 11%-thick BAC3-11/RES/30/21 supercritical airfoil. The inboard section uses the same airfoil thickened linearly from 11% at its outer edge to 15% at the root. To minimize boundary-layer interference during testing, a generic fuselage was included. It extended 0.09 meters from the tunnel ceiling and was mechanically isolated from the wing by a labyrinth seal. Boundary-layer transition strips were affixed to the upper wing surface at 12-15% chord and to the lower surface at 5% chord for portions of the test. Extensive measurements were acquired during testing of the HIRENASD model. Instrumentation included a six-component balance, surface pattern tracking (SPT) optical markers for surface deformation measurements on the pressure side of the wing, 11 accelerometers, 28 strain gages, and 259 unsteady pressure transducers. The pressure transducers were distributed along the upper and lower surfaces at the seven span sections shown in Figure 5b.

The HIRENASD test matrix consisted of both static and dynamic measurements acquired at different flow conditions, with variations of Reynolds number from 7 million up to 73 million based on the mean aerodynamic chord and dynamic pressures up to 130,000 Pascals at six transonic Mach numbers: 0.70, 0.75, 0.80, 0.83, 0.85, and 0.88. The test medium at ETW was nitrogen. For static testing, pressure distribution and lift and drag coefficients were acquired during angle-of-attack polars, where the angle of attack was slowly varied at an angular sweep rate of 0.2 degrees per second, holding all other operational parameters constant. Dynamic testing involved forced oscillations of the wing via differential forcing at or near one of three of the wing′s natural frequencies: the first bending mode at approximately 27 Hz, the second bending mode at approximately 79 Hz, or the first torsion mode at approximately 265 Hz.

For AePW, six test cases were selected for the HIRENASD computational challenge, as shown in Table 5. The first, second, and fifth were steady (static aeroelastic) cases, while the third, fourth, and sixth were dynamic cases at test conditions corresponding to the static cases. All forced oscillation data used in AePW involved excitation near the wing′s second bending mode frequency. Two Mach numbers, 0.70 and 0.80, were selected for analysis, corresponding to cases five and six and one through four, respectively. Two Reynolds numbers, 7.0 million and 23.5 million based on reference chord, were also selected. Four of the six test cases called for analyses using the lower Reynolds number at an angle of attack of 1.5 degrees. Two of the cases (one static and one dynamic) at the higher Mach number called for additional analyses with the higher Reynolds number at a more challenging angle of attack of -1.34 degrees, corresponding to the zero-lift condition. For workshop test cases at 7.0 million, the boundary layer transition strips were affixed to the upper surface of the wing at 12-15% chord and on the lower surface at 5% chord.

FUN3D analyses were performed for all six HIRENASD test cases. The solutions on three grid resolutions (coarse, medium, and fine) were obtained for the higher Mach number cases (1-4), while solutions for the lower Mach number cases (5-6) were obtained using two grid resolutions (coarse and medium). The fine-grid solution for the lower Mach number did not converge to the satisfactory levels. In this paper, the HIRENASD results presented will focus on comparing FUN3D static aeroelastic computational results with the corresponding experimental data from HIRENASD experiment Nos. 159, 155, and 271 and comparing FUN3D dynamic results with HIRENASD experiment No. 159 only, where the model was harmonically excited at the second bending mode frequency. The finite element model and the issues encountered with interpolating the mode shapes to the surface mesh are discussed first. The rigid steady

and static aeroelastic results are then compared together against the corresponding experimental data, and finally, the harmonic excitation computational results will be compared against experimental data.

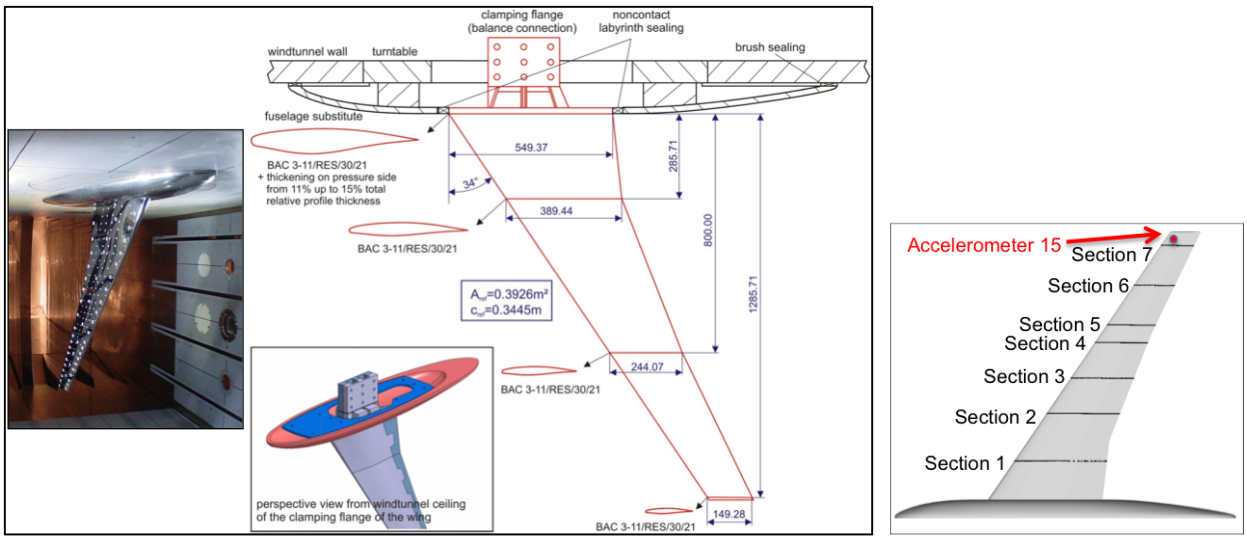

(a) HIRENASD wing model planform, assembly, and ETW installation photo. (Dimensions shown are in millimeters.)

(b) HIRENASD experimental sections.

Figure 5. HIRENASD wing model planform and span sections 1-7 with accelerometer 15 location.

Table 5. HIRENASD Analysis Test Cases.

Test Case	Mach No.	Mean α (deg)	Forcing Freq. (f, Hz)	Modal Amp. at Accel. 15 (m)	Reduced Freq. ω c / $2V_\infty$	Re_c $*10^6$	ETW Test No.
1	0.8	1.5	0	0.0	0.000	7	159
2	0.8	-1.34	0	0.0	0	23.5	271
3	0.8	1.5	78.9	0.0024	0.333	7	159
4	0.8	-1.34	80.4	0.0009	0.396	23.5	271
5	0.7	1.5	0	0.0	0	7	155
6	0.7	1.5	79.3	0.0020	0.378	7	155

A. Finite Element Model

The MSC Nastran^{TM} FEM of the HIRENASD configuration used for AePW is a modified version of the model provided by Aachen University.[28] The modifications include instrumentation masses, better bolt connections, and the ability to measure the deflections at the accelerometer locations. The result is a very detailed model, containing over 200,000 uniform solid hexagonal elements in the wing alone. Specific details of the FEM will be described in future publications. Modal analyses were performed on the modified FEM, and the first 29 modes were extracted and used in the aeroelastic analyses presented in this paper. Unfortunately, the FEM and the wing/fuselage surface available from Aachen University did not align perfectly. In addition, the grids for the CFD calculations were constructed prior to FEM completion. Consequently, the FEM's outer model line grids were projected to the surfaces used in grid generation and used in structural analysis.

B. Static-Aeroelastic Solution

As described in Section II B, the rigid steady solutions were obtained first. These solutions were then used as initial conditions for the corresponding static aeroelastic solutions (Section II C), which in turn were obtained by running FUN3D in the unsteady flow mode with the modal structural solver, where the structural damping value was set to

a large value. The solution process required that the mode shapes be interpolated to the surface grid. Two sets of solutions were obtained, one without the flux limiter and the second one with the flux limiter. The mode shapes were interpolated to both the wing and the fuselage. The modes shapes were then set to zero on the fuselage, with the exception of a very narrow region near the wing and fuselage junction. This process eliminated a discontinuity in mode shape at this junction. Figure 6 shows the second bending mode 2 both as an output shape from the modified FEM and as interpolated onto the CFD surface grid.

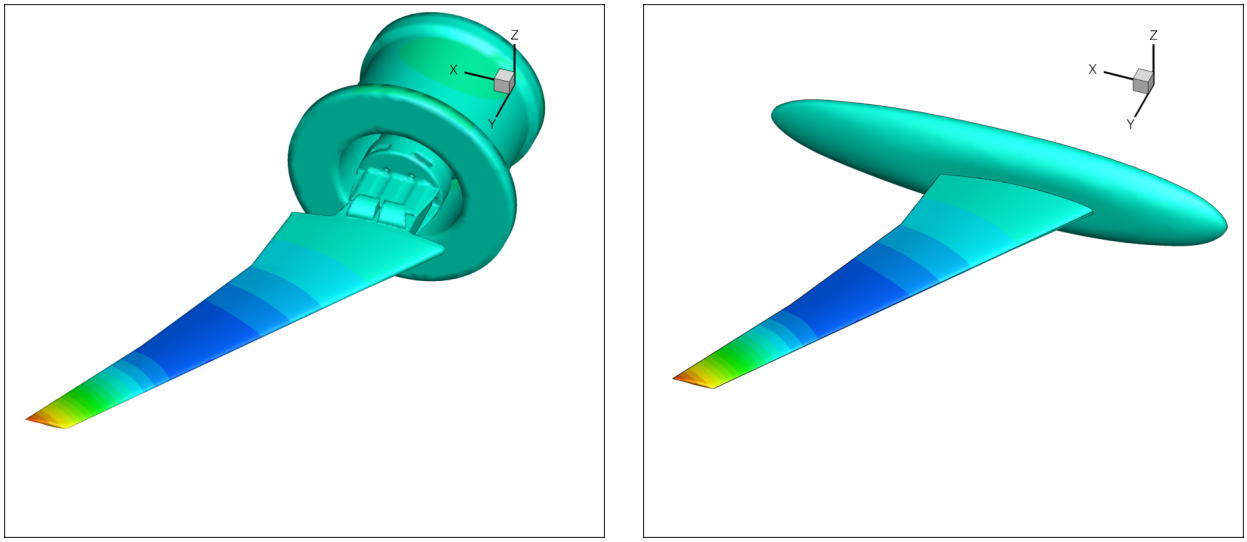

(a) Second bending mode from FEM.

(b) Second bending mode interpolated on CFD mesh.

Figure 6. Example of the mode shape interpolation process from FEM into CFD surface mesh for the HIRENASD configuration.

The aerodynamic coefficients obtained from both the rigid steady and static aeroelastic calculations for the coarse, medium, and fine grids are shown in Table 6 where FUN3D solutions were obtained without flux limitation and in Table 7 where FUN3D solutions were obtained with flux limitation. In general, a very small decrease in computed drag coefficient is observed among the grids. Also, a small lift decrement exists between the rigid steady and deformed (static aeroelastic) configurations. The lift coefficients are also plotted versus grid factor $N^{-2/3}$, where N is number of grid points, in Figure 7. The differences in computed lift coefficient between solutions with and without flux limitation are significant and consistent with other FUN3D analyses.[29] These differences are also higher than the differences between rigid and static aeroelastic solutions. Note that for plotting simplicity, the fine-grid results at Re_c = 7 million and Mach = 0.7 is included in in Figure 7 even though the solution did not converge to the satisfactory levels.

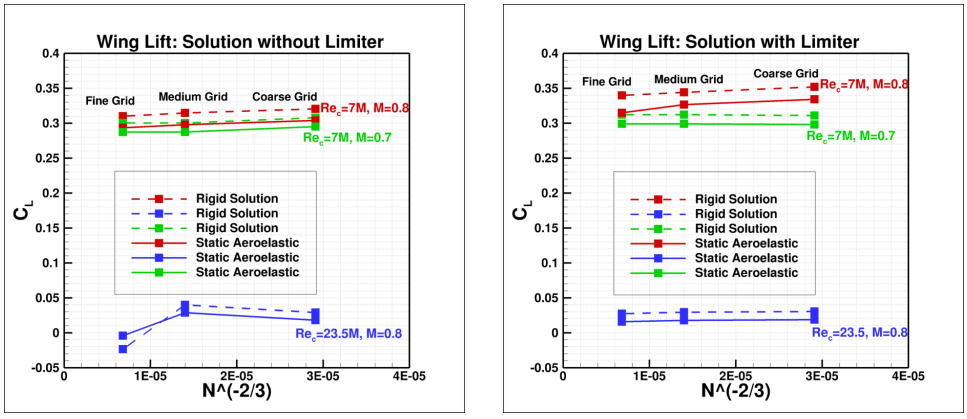

(a) Lift coefficient vs. grid factor: Solution without flux limitation.

(b) Lift coefficient vs. grid factor: Solution with flux limitation.

Figure 7. FUN3D solutions with and without flux limitation.

Table 6. Computed Aerodynamic Coefficients for Coarse/Medium/Fine Grids (Rigid Steady and Deformed Solutions): HIRENASD Test Case Nos. 159, 271, 155. FUN3D Solution without Flux Limiter

	Rigid Steady Solution			Static Aeroelastic Solution		
Case 159	C_L	C_D	C_M	C_L	C_D	C_M
Coarse Grid	0.3204	0.0145	-0.2754	0.3038	0.0139	-0.2594
Medium Grid	0.3145	0.0145	-0.2729	0.2979	0.0139	-0.2571
Fine Grid	0.3099	0.0142	-0.2697	0.2935	0.0136	-0.2540
	Rigid Steady Solution			Static Aeroelastic Solution		
Case 271	C_L	C_D	C_M	C_L	C_D	C_M
Coarse Grid	0.0291	0.0093	-0.0954	0.0180	0.0095	-0.0851
Medium Grid	0.0401	0.0105	-0.0929	0.0289	0.0107	-0.0824
Fine Grid	-0.0233	0.0093	-0.1322	-0.0041	0.0109	0.0735
	Rigid Steady Solution			Static Aeroelastic Solution		
Case 155	C_L	C_D	C_M	C_L	C_D	C_M
Coarse Grid	0.3077	0.0117	-0.2492	0.2951	0.0113	-0.2371
Medium Grid	0.3003	0.0118	-0.2469	0.2874	0.0115	-0.2352

Table 7. Computed Aerodynamic Coefficients for Coarse/Medium/Fine Grids (Rigid Steady and Deformed Solutions): HIRENASD Test Case Nos. 159, 271, 155. FUN3D Solution with Flux Limiter

	Rigid Steady Solution			Static Aeroelastic Solution		
Case 159	C_L	C_D	C_M	C_L	C_D	C_M
Coarse Grid	0.3520	0.0152	-0.2931	0.3342	0.0145	-0.2759
Medium Grid	0.3440	0.0149	-0.2900	0.3266	0.0142	-0.2732
Fine Grid	0.3398	0.0152	-0.2913	0.3149	0.0141	-0.2679
	Rigid Steady Solution			Static Aeroelastic Solution		
Case 271	C_L	C_D	C_M	C_L	C_D	C_M
Coarse Grid	0.0306	0.0098	-0.0967	0.0188	0.0099	-0.0857
Medium Grid	0.0295	0.0093	-0.0959	0.0179	0.0095	-0.0851
Fine Grid	0.0274	0.0093	-0.0952	0.0159	0.0094	-0.0843
	Rigid Steady Solution			Static Aeroelastic Solution		
Case 155	C_L	C_D	C_M	C_L	C_D	C_M
Coarse Grid	0.3109	0.0123	-0.2523	0.2981	0.0119	-0.2398
Medium Grid	0.3122	0.0118	-0.2535	0.2991	0.0118	-0.2409

Figures 8, 9, and 10 present C_p results at all seven wing sections and compares the results with the experimental data. The computed C_p matches the experimental data quite well. The largest discrepancy between the experimental and computational data can be observed at wing sections 1 and 7. The computational data at wing section 1 is either affected by the recirculation region at the wing-fuselage junction or by the proximity of this section to the wind-tunnel wall. The computational data at wing section 7 is affected by the wing-tip effects.

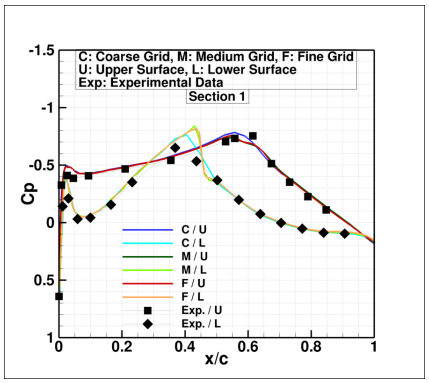

(a) Section 1.

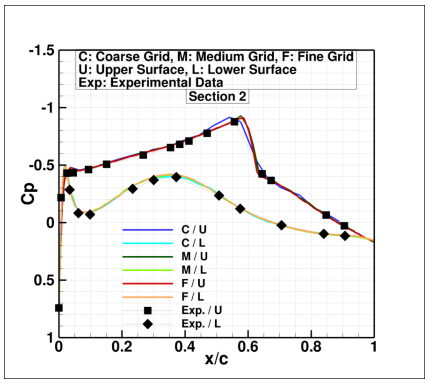

(b) Section 2.

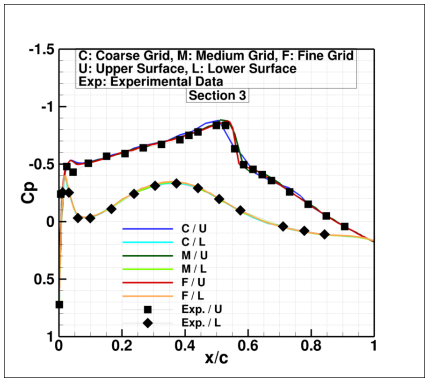

(c) Section 3.

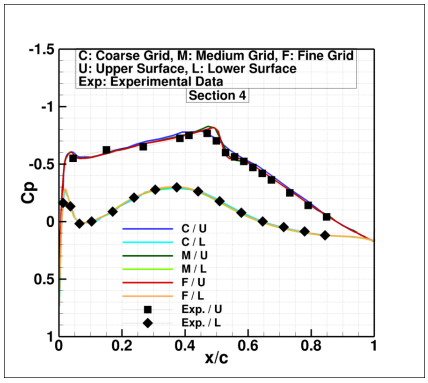

(d) Section 4.

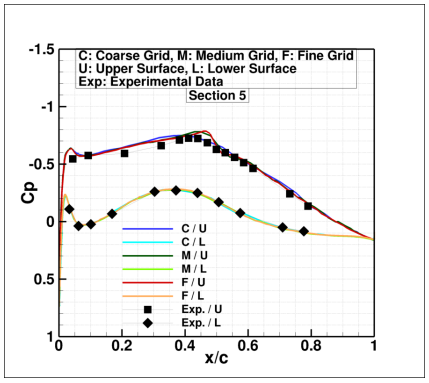

(e) Section 5.

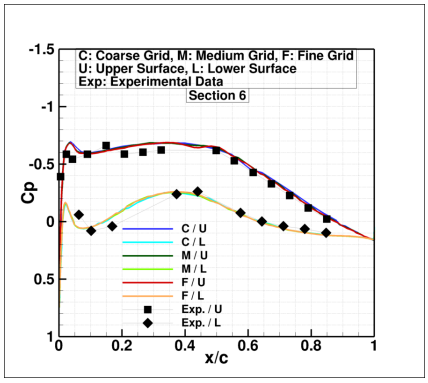

(f) Section 6.

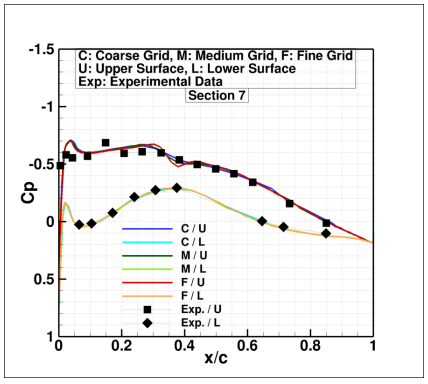

(g) Section 7.

Figure 8. Static aeroelastic surface pressure comparison for coarse/medium/fine grids at wing sections 1-7 for HIRENASD test case No. 159, Mach = 0.8, Re_c = 7 * 10^6.

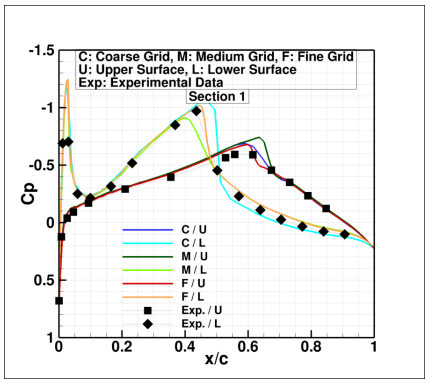

(a) Section 1.

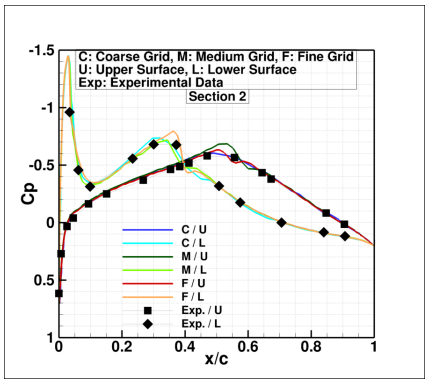

(b) Section 2.

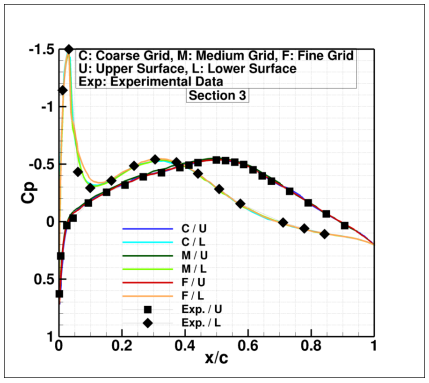

(c) Section 3.

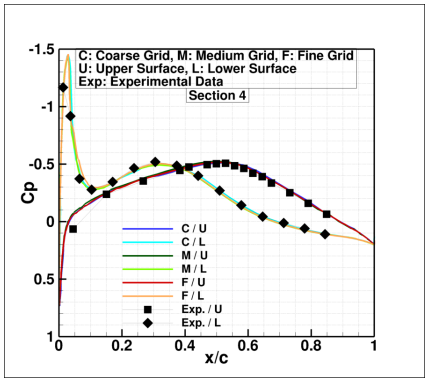

(d) Section 4.

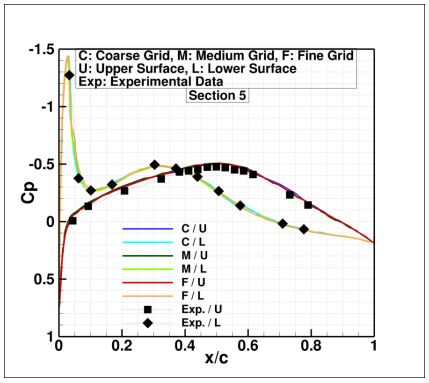

(e) Section 5.

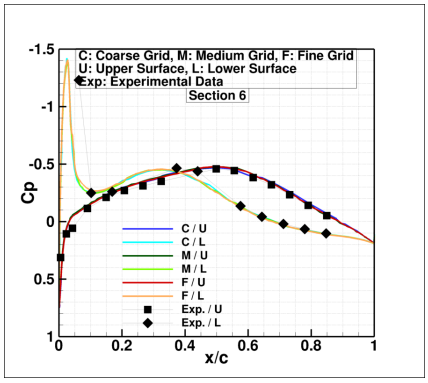

(f) Section 6.

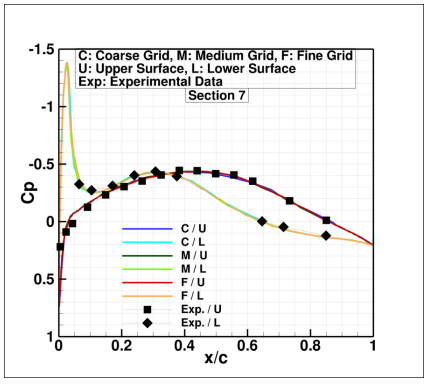

(g) Section 7.

Figure 9. Static aeroelastic surface pressure comparison for coarse/medium/fine grids at wing sections 1-7 for HIRENASD test case No. 271, Mach = 0.80, Re_c = 23.5 * 10^6.

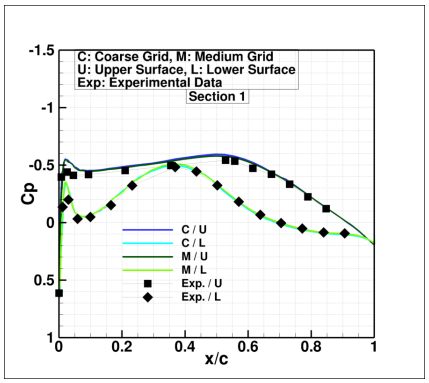

(a) Section 1.

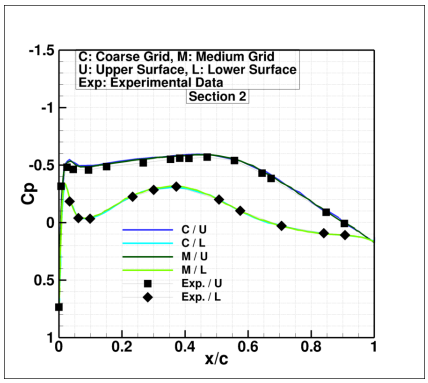

(b) Section 2.

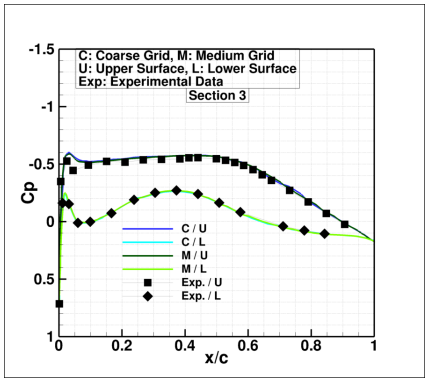

(c) Section 3.

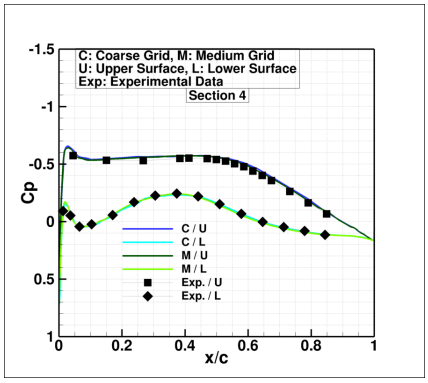

(d) Section 4.

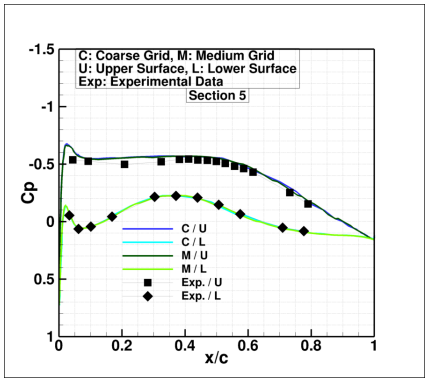

(e) Section 5.

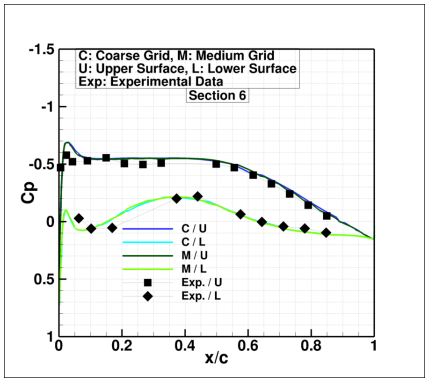

(f) Section 6.

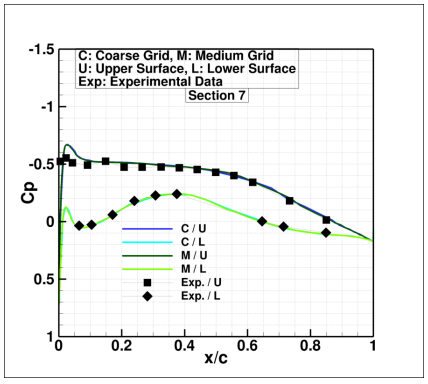

(g) Section 7.

Figure 10. Static aeroelastic surface pressure comparison for coarse/medium grids at wing sections 1-7 for HIRENASD test case No. 155, Mach = 0.70, Re_c = 7 * 10^6.

C. Forced Excitation Solution

The HIRENASD experimental harmonic excitation tests were conducted to measure the interaction between aerodynamics and modal excitations of the wing. The forcing frequencies associated with the AePW test cases are shown in Table 5. Numerically, the modal excitation is accomplished using Equation 4. The unsteady solutions were restarted from the static aeroelastic solutions and were run for six cycles, with 64 time steps per cycle and the temporal convergence error set to 5%. The prescribed convergence was reached within 35 to 75 subiterations per time step, depending on the grid resolution. The unsteady surface pressure and surface shape were collected at each time step for four cycles. The results were post-processed to produce the FRF of pressure due to displacement at a specified location. The displacement location used in the analysis coincided with the location of accelerometer 15, which is shown in Figure 5b. The displacement value was normalized by the reference chord. Figures 11, 12, 13, and 14 show the resulting C_p magnitude and phase plots for the upper and lower surfaces, for wing sections 1 through 7 for the coarse, medium, and fine grids. The shock locations at wing sections 1-5 are predicted quite well, but the prediction is poor near the wing tip.

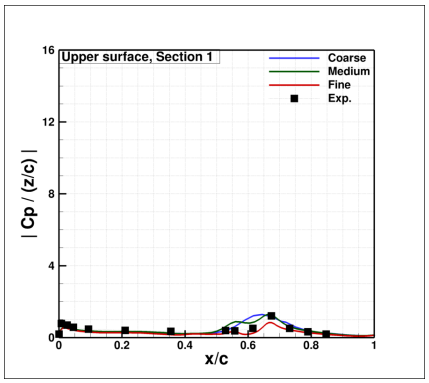

(a) Section 1.

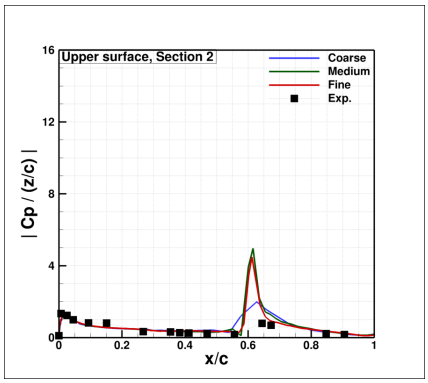

(b) Section 2.

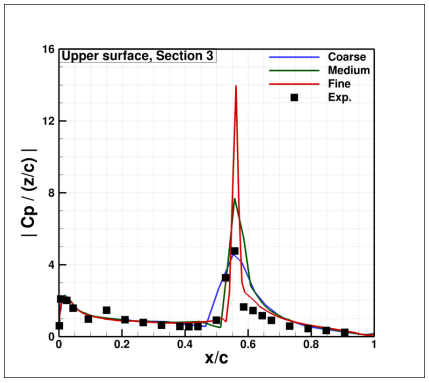

(c) Section 3.

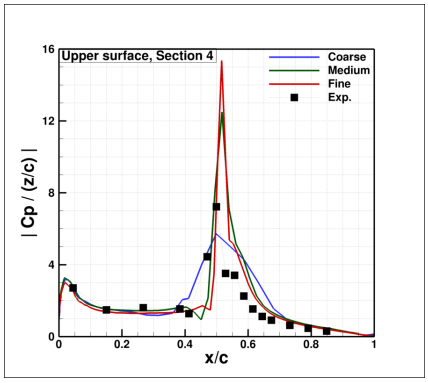

(d) Section 4.

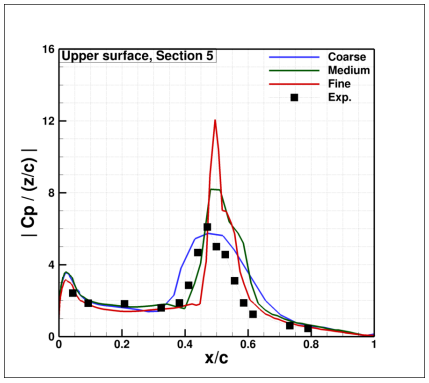

(e) Section 5.

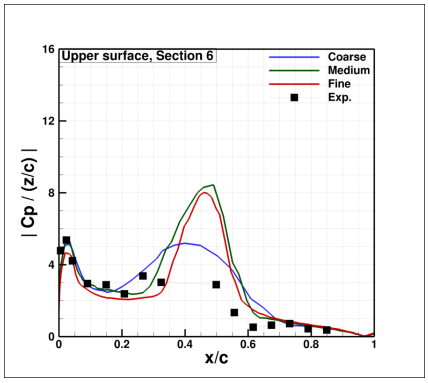

(f) Section 6.

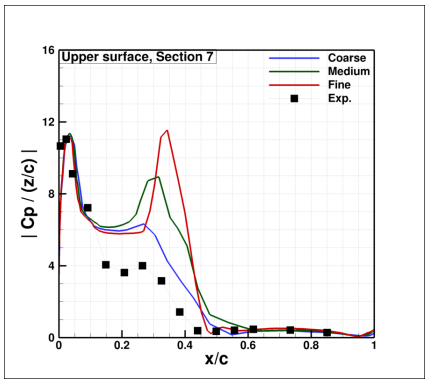

(g) Section 7.

Figure 11. Frequency Response Function: Magnitude of the pressure coefficient due to the displacement at accelerometer 15 for coarse, medium, and fine grids; HIRENASD test case 159, upper surface.

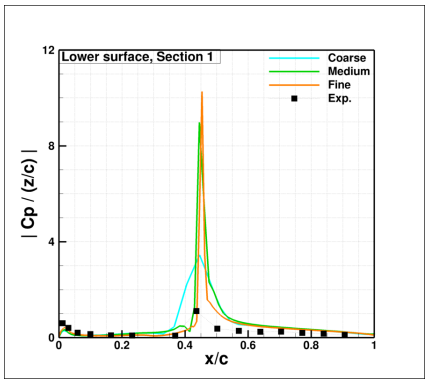

(a) Section 1.

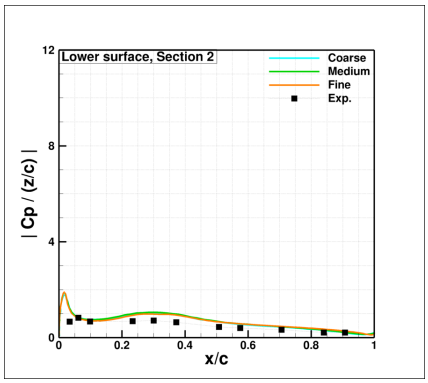

(b) Section 2.

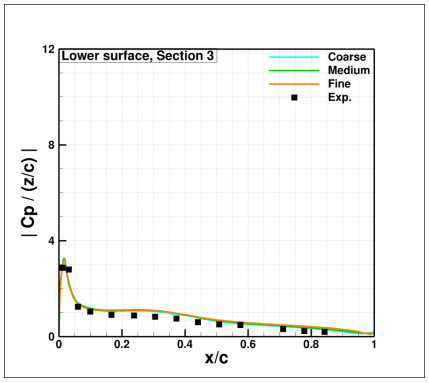

(c) Section 3.

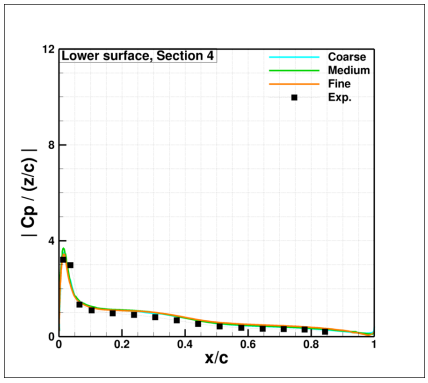

(d) Section 4.

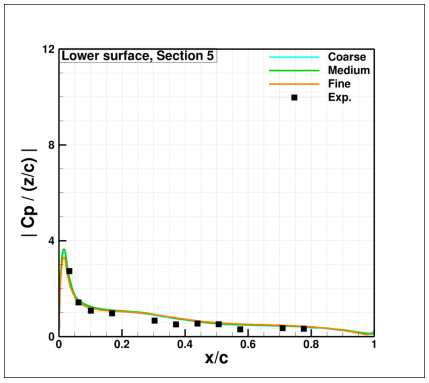

(e) Section 5.

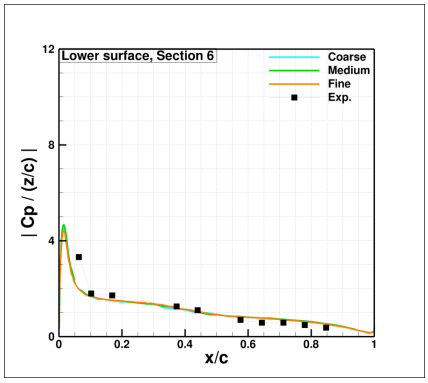

(f) Section 6.

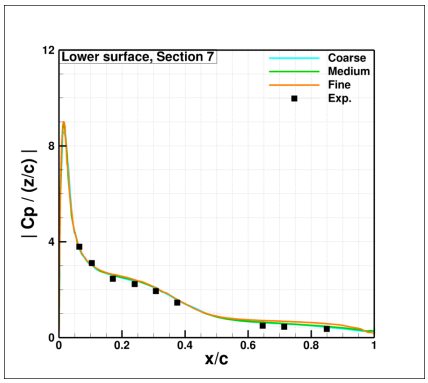

(g) Section 7.

Figure 12. Frequency Response Function: Magnitude of the pressure coefficient due to the displacement at accelerometer 15 for coarse, medium, and fine grids; HIRENASD test case 159, lower surface.

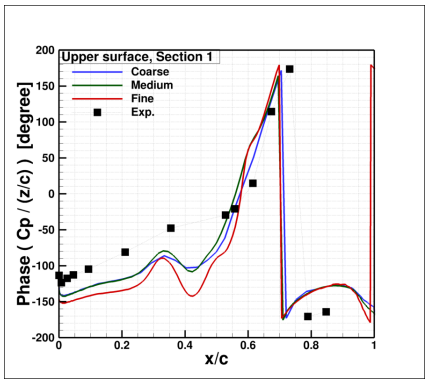

(a) Section 1.

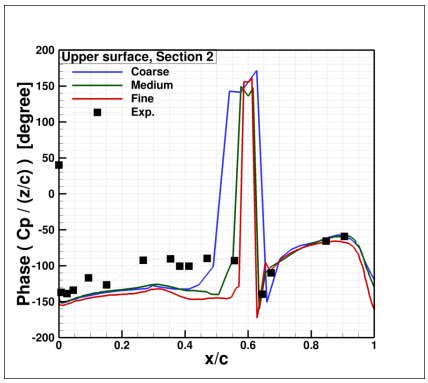

(b) Section 2.

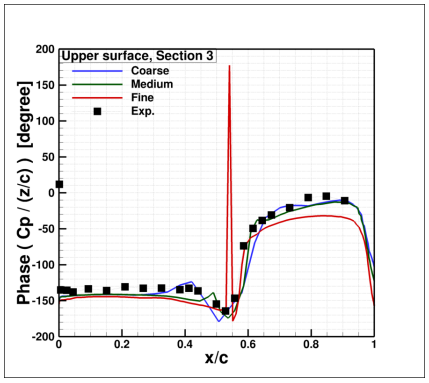

(c) Section 3.

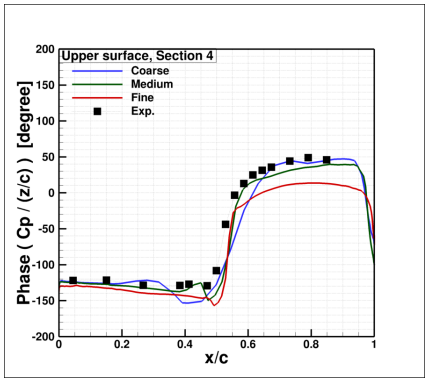

(d) Section 4.

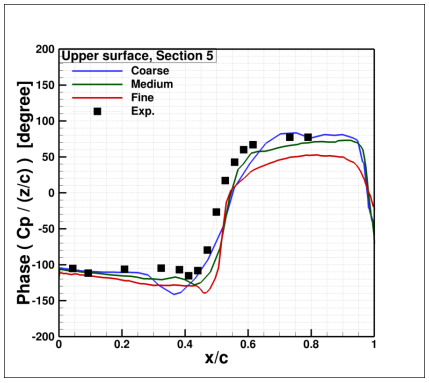

(e) Section 5.

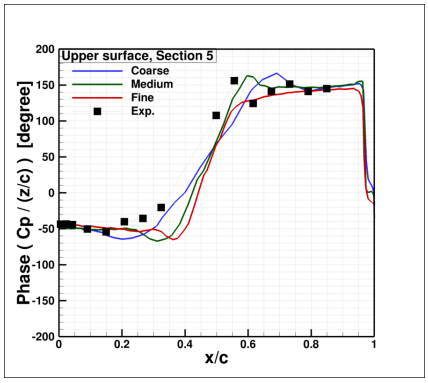

(f) Section 6.

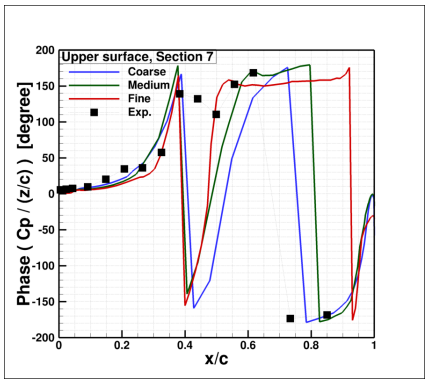

(g) Section 7.

Figure 13. Frequency Response Function: Phase of the pressure coefficient due to the displacement at accelerometer 15 for coarse, medium, and fine grids; HIRENASD test case 159, upper surface.

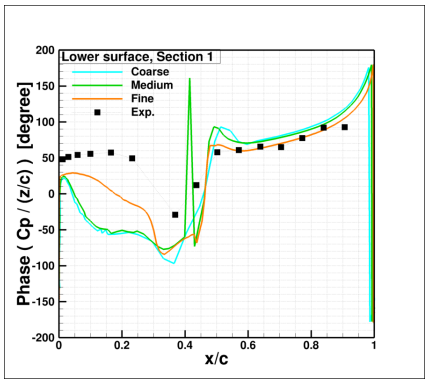

(a) Section 1.

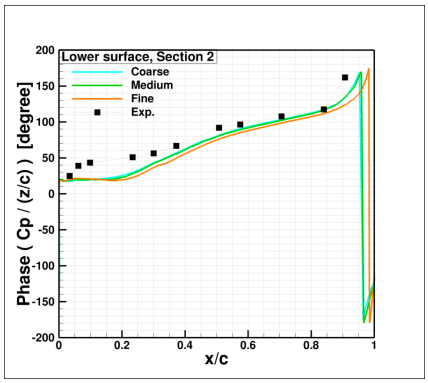

(b) Section 2.

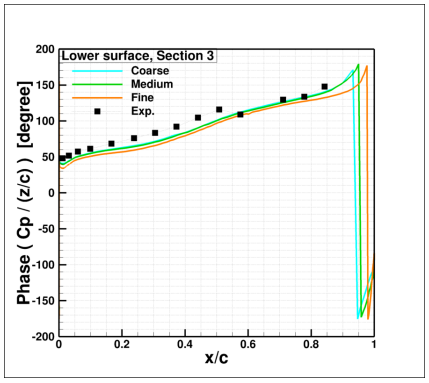

(c) Section 3.

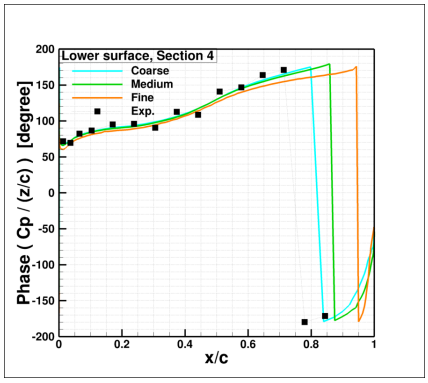

(d) Section 4.

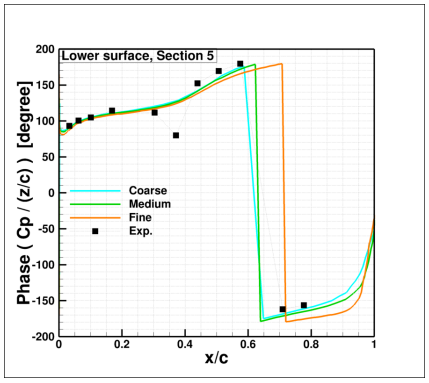

(e) Section 5.

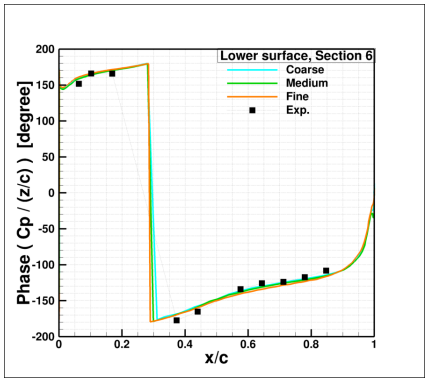

(f) Section 6.

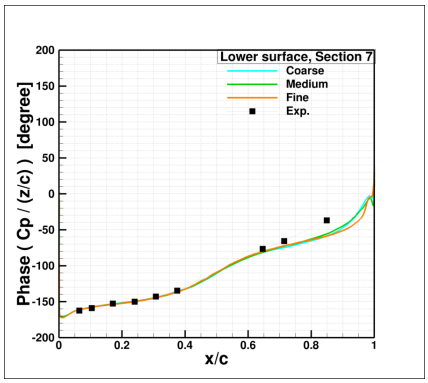

(g) Section 7.

Figure 14. Frequency Response Function: Phase of the pressure coefficient due to the displacement at accelerometer 15 for coarse, medium, and fine grids; HIRENASD test case 159, lower surface.

V. Concluding Remarks

Reynolds-averaged Navier-Stokes analyses, including steady state, static aeroelastic, and forced excitation, were performed as part of AePW using the NASA Langley FUN3D software. The analyses were performed on all configurations and cases considered for the workshop. This paper presented complete results for the BSCW configuration and partial results for the HIRENASD configuration. In both cases, aerodynamic coefficients from the steady-state analysis were reported. With the HIRENASD case, aerodynamic coefficients from the static-aeroelastic analysis were provided as well. The frequency response function of pressure due to displacement was calculated for the forced pitching and modal oscillations and compared with the experimental data.

For the BSCW configuration, the computed shock location was located aft of the experimentally-measured shock. This was indicated by the mean pressure distribution and the frequency response functions. Clearly, RANS analysis at 5-degrees angle of attack did not produced experimentally matching pressure behind the shock in the flow-separated region.

For the HIRENASD configuration, there was a very good match between the experimental and numerical data. The largest discrepancies in surface pressure were observed at the most inboard and outboard sections. It was hypothesized that the experimental pressure at the inboard section might have been affected by the proximity of the wind-tunnel wall, which was not modeled. The pressure collected at the most outboard section might have been affected by the wing-tip effects, which in general are difficult to predict numerically.

Acknowledgments

The authors gratefully acknowledge the AePW team at NASA Langley and the entire AePW Organizing Committee for their guidance and discussions. The authors would also like to acknowledge Dr. Jamshid Samareh of NASA Langley for his help in setting up the mode shape interpolation process.

References

[1]Yates, C. E., Land, N. S., and Foughner, J. T., "Measured and Calculated Subsonic and Transonic Flutter Characteristics of a 45deg Sweptback Wing Planform in Air and in Freon-12 in the Langley Transonic Dynamics Tunnel," NASA Technical Note D-1616, March 1963.

[2]Yates, C. E., "AGARD Standard Aeroelastic Configurations for Dynamic Response - Wing 445.6," AGARD Report No. 765, July 1988.

[3]Bennett, R. M. and Edwards, J. W., "An Overview of Recent Developments in Computational Aeroelasticity," AIAA Paper 1998-2421, June 1998.

[4]"http://aaac.larc.nasa.gov/tsab/cfdlarc/aiaa-dpw/".

[5]"http://hiliftpw.larc.nasa.gov/".

[6]Ricketts, R. H., Sandford, M. C., Watson, J. J., and Seidel, D. A., "Geometric and Structural Properties of a Rectangular Supercritical Wing Oscillated in Pitch for Measurement of Unsteady Trnasonic Pressure Distributions," NASA TM 1983-85763, Nov. 1983.

[7]Ricketts, R. H., Sandford, M. C., Seidel, D. A., and Watson, J. J., "Transonic Pressure Distributions on a Rectangular Supercritical Wing Oscillating in Pitch," NASA TM 1983-84616', March 1983.

[8]Ricketts, R. H., Sandford, M. C., Watson, J. J., and Seidel, D. A., "Subsonic and Transonic Unsteady and Steady-Pressure Measurements on a Rectangular Supercritical Wing Oscillated in Pitch," NASA TM 1984-85765, Nov. 1984.

[9]Bennett, R. M. and Walker, C. E., "Computational Test Cases for a Rectangular Supercritical Wing Undergoing Pitching Oscillations," NASA TM 1984-209130, April 1999.

[10]Piatak, D. J. and Cleckner, C. S., "A New Forced Oscillation Capability for the Transonic Dynamics Tunnel," AIAA Paper 2002-0171, Jan. 2002.

[11]Ballmann, J., Dafnis, A., Korsch, H., Buxel, C., Reimerdes, H.-G., Brakhage, K.-H., Olivier, H., Braun, C., Baars, A., and Boucke, A., "Experimental Analysis of High Reynolds Number Aero-Structural Dynamics in ETW," AIAA Paper 2008-841, Jan. 2008.

[12]Ballmann, J., Boucke, A., Dickopp, C., and Reimer, L., "Results of Dynamic Experiments in the HIRENASD Project and Analysis of Observed Unsteady Processes," IFASD Paper 2009-103, June 2009.

[13]Ballmann, J., Dafnis, A., Braun, C., Korsch, H., Reimerdes, H.-G., and Olivier, H., "The HIRENASD Project: High Reynolds Number Aerostructural Dynamics Experiments in the European Transonic Windtunnel (ETW)," ICAS Paper 2006-726, Sept. 2006.

[14]"http://fun3d.larc.nasa.gov", NASA Langley Research Center, November 2010.

[15]Pirzadeh, S. Z., "Advanced Unstructured Grid Generation for Complex Aerodynamic Applications," AIAA Paper 2008–7178, Aug. 2008.

[16]Samareh, J. A., "Unstructured Grids on NURBS Surfaces," AIAA Paper 1993–3454.

[17]"https://c3.nasa.gov/dashlink/projects/47/".

[18]Spalart, P. R. and Allmaras, S. R., "A One-Equation Turbulence Model for Aerodynamic Flows," *La Recherche Aerospatiale*, No. 1, 1994, pp 5–21.

[19]Venkatakrishnan, V., "Convergence to Steady State Solutions of the Euler Equations on Unstructured Grids with Limiter," *Journal of Computational Physics*, Vol. 118, No. 1, 1995.

[20]Roe, P. L., "Approximate Riemann Solvers, Parameter Vectors, and Difference Schemes," *Journal of Computational Physics*, Vol. 43, No. 2, 1981.

[21]Biedron, R. T. and Thomas, J. L., "Recent Enhancements to the FUN3D Flow Solver for Moving-Mesh Applications," AIAA Paper 2009-1360, Jan. 2009.

[22]Biedron, R. T. and Lee-Rausch, E. M., "Rotor Airloads Prediction Using Unstructured Meshes and Loose CFD/CSD Coupling," AIAA Paper 2008-7341, 2008.

[23]Batina, J. T., "Unsteady Transonic Flow Calculations for Realistic Aircraft Configurations," AIAA Paper 1987-0850, 1987.

[24]Bartels, R. E., Rumsey, C. L., and Biedron, R. T., "CFL3D Version 6.4 - General Usage and Aeroelastic Analysis," NASA TM 2006-214301, March 2006.

[25]MSC Software, Santa Ana, CA, *MSC Nastran*, 2008, http://www.mscsoftware.com/products/msc_nastran.cfm.

[26]Samareh, J. A., "Discrete Data Transfer Technique for Fluid-Structure Interaction," AIAA Paper 2007–4309, June 2007.

[27]Schuster, D. M., "Aerodynamic Measurements on a Large Splitter Plate for the NASA Langley Trnasonic Dynamics Tunnel," NASA TM 2001-210828, March 2001.

[28]"https://heinrich.lufmech.rwth-aachen.de/en/", Aachen University.

[29]Park, M. A. et al., "FUN3D, NSU3D, and CFL3D Contributions to the Fifth Drag Prediction Workshop," AIAA Paper 2013, Jan. 2013.